ADVANCED ELECTRONIC MATERIALS
www.advelectronicmat.de

Properties and Applications of Copper(I) Thiocyanate Hole-Transport Interlayers Processed from Different Solvents

*Bingjun Wang, Sungho Nam, Saurav Limbu, Ji-Seon Kim, Moritz Riede, and Donal D. C. Bradley**

Copper(I) thiocyanate (CuSCN) is an effective interlayer material for hole injection and transport in organic electronic devices but its solution processing has conventionally utilized undesirable di-*n*-alkyl sulfide solvents such as diethyl- (DES) and dipropyl-sulfide (DPS). Herein, this paper reports on the use of *N*,*N*-dimethylformamide (DMF) and 1-methyl-2-pyrrolidinone (NMP) as alternative solvents for CuSCN interlayers and performs a detailed comparison of the resulting properties relative to films processed from DES and DPS and two other recent alternatives, dimethyl sulfoxide (DMSO) and ammonium hydroxide. The surface roughness, polymorphism, and surface chemistry of the resulting CuSCN layers are reported. The interlayer surface energy and ionization potential that are key to the overlying semiconductor microstructure and interfacial energy barrier, and hence to charge transport and injection, are also discussed. Finally, systematic device tests using well-known organic semiconductors in light-emitting diode, solar cell and field-effect transistor structures demonstrate the overall suitability of DMSO and DMF as solvents for CuSCN interlayer deposition to achieve better device performance. This study broadens the applicability of CuSCN as a highly efficient hole injection/transport material for organic semiconductor devices by expanding the documented range of suitable CuSCN solvents.

1. Introduction

Organic semiconductor devices have witnessed rapid developments across multiple device types in recent years, from the commercial success of organic light-emitting diode (OLED)-based display technology that followed pioneering work three decades ago,[1] to organic solar cells (OSCs) now able to convert more than 18% of incident solar energy to electricity,[2] and organic field-effect transistors (OFETs) approaching comparable mobility to polycrystalline silicon and metal-oxide FETs.[3] These achievements largely originate from an evolution in organic semiconducting materials, deeper understanding of the associated device physics, and a proliferation of device engineering expertise. One widely applied element of device engineering is the insertion of appropriate interlayers within the device stack,[4] in order to tune interfacial physical and chemical processes and the heterojunction energy structure.[5]

Conventionally, interlayers in organic electronic devices are broadly categorized as electron-injection/transport layers (EILs/ETLs) or hole-injection/transport layers (HILs/HTLs),[4] depending on the charge carrier type for which injection and/or transport is facilitated. These injection and transport layers can also serve, importantly, as blocking layers for the opposite sign of charge carrier,[6] avoiding the need for separate charge blocking layers. Both injecting and blocking properties are determined by the energy level alignments between the interlayers and active materials, also taking into account any dipole induced offsets in the vacuum level.[7] In addition, an optical gap larger than

B. Wang, S. Nam, M. Riede, D. D. C. Bradley
Clarendon Laboratory
Department of Physics
University of Oxford
Oxford OX1 3PU, UK
E-mail: donal.bradley@kaust.edu.sa

The ORCID identification number(s) for the author(s) of this article can be found under https://doi.org/10.1002/aelm.202101253.

DOI: 10.1002/aelm.202101253

S. Nam
Samsung Advanced Institute of Technology (SAIT)
Samsung Electronics Co., Ltd.
130 Samsung-ro, Suwon-si, Gyeonggi-do 16678, Republic of Korea

S. Limbu, J.-S. Kim
Department of Physics and Centre for Processable Electronics
Blackett Laboratory
Imperial College London
London SW7 2AZ, UK

D. D. C. Bradley
Physical Science and Engineering Division
King Abdullah University of Science and Technology (KAUST)
Thuwal 23955-6900, Saudi Arabia

that of the active materials in the device is generally important for interlayers in OSCs and OLEDs since their competing light absorption is, respectively, unfavorable to light harvesting and emission efficiencies. Last but not least, facile deposition with good film forming characteristics (even at low layer thickness) is a serious practical concern. This requires that the deposition does not damage any underlying layers, avoids formation of pinholes and other defects, results in spatially uniform surface properties, and yields good adhesion to materials both below and on top.

Compared with a large number of available EILs/ETLs,[8] choices for solution-processable HILs/HTLs primarily focus on poly(3,4-ethylenedioxythiophene):poly(styrene sulfonate) (PEDOT:PSS) and materials developed therefrom,[9] together with various inorganic materials such as transition metal oxides.[10] As a mixture of conductive PEDOT-decorated PSS chains and insulating undecorated PSS chains,[11] PEDOT:PSS combines good solubility and processability, tunable conductivity,[12] and a work function (WF) of ≈5.2 eV, comparable to or higher than that of typical indium tin oxide (ITO).[13] These desirable features, which have driven very widespread utilization, are offset to some degree by the acidity and chemical reactivity of the films[14] and the potential for de-doping accompanied by detachment of the PEDOT segments from their PSS carrier chains. This is further compounded by a non-negligible absorption in the visible spectral range.[15] In addition, the electron-blocking properties of PEDOT:PSS are not ideal,[16] and the tendency for electrons to be trapped by PEDOT:PSS (also leading to de-doping) can cause changes in device performance over time.[17] The PEDOT:PSS WF is also insufficient to generally support ohmic injection into materials with larger ionization potential values (IP ≥ 5.5eV), leading to hole-injection-limited electrode function,[18] albeit that in certain circumstances Fermi level pinning at the interface can remove this barrier.[19] Moreover, the WF of PEDOT:PSS is found to be sensitive to processing protocols,[13] as its microstructure and surface composition may vary.[20] These considerations have led, over a number of years, to an active search for PEDOT:PSS replacements, with efforts mainly focused on inorganic hole-injection/transport materials. It has not, however, proven straightforward to achieve this objective.

Commonly used examples of inorganic HILs/HTLs include MoO_3, WO_3, and V_2O_5, all with higher WFs than PEDOT:PSS.[21] The limiting factors then change to fabrication conditions, since thermal evaporation is usually preferred for these materials. Although solution-processing methods are possible,[22] the mechanism of in situ thermal decomposition of the precursor layer[23] normally requires high annealing temperatures,[10] with the possibility of ending up with an interlayer showing unfavorable stoichiometry and, consequently, energetics should, for example, substrate temperature limits intervene.[24] A more recent option for use as an HIL/HTL is copper(I) thiocyanate (CuSCN), which is inexpensive, abundantly available,[15a] and readily soluble in di-*n*-alkyl sulfides such as diethyl sulfide (DES) and dipropyl sulfide (DPS).[25] The calculated band structure of CuSCN[26] supports its potential for use as a hole-injection/transport material, with its large optical band gap (≈3.8 eV) yielding high transparency, a deep-lying valence band edge (around −5.8 eV) for effective hole injection, and a low-lying conduction band edge (around −2.1 eV) for good electron blocking. Solution-processed CuSCN interlayers have been used to good effect in OLEDs, OSCs and transistors.[15,27] The limited choices of solvent for CuSCN are, however, an impediment to its wider application. In particular, DES and DPS are hazardous chemicals of long-lasting, unpleasant odor, and their use demands specific care and control.

To overcome this limitation, researchers have sought to find new solvents for CuSCN which need both to be more benign and to ensure that the deposited CuSCN interlayers have hole injection/transport properties as good as, if not better than, films processed from the benchmark solvents, DES and DPS. Wijeyasinghe et al.[27d] reported the use of ammonium hydroxide (NH_4OH) to dissolve CuSCN. The resulting thin films showed lower surface roughness, deeper valence band edge, and better environmental stability than DES-based counterparts. In comparison with PEDOT:PSS, improved efficiencies were observed for both OSCs and perovskite solar cells using NH_4OH-processed CuSCN as a substitute interlayer. Chaudhary et al.[27e] further showed that dimethyl sulfoxide (DMSO) can also dissolve CuSCN, and reported the use of DMSO-processed CuSCN interlayers in OSCs. To date, DES, DPS, NH_4OH and DMSO appear to be the only solvents that have been used to solution-process CuSCN interlayers for organic semiconductor devices.

In this report we present a side-by-side comparison of these known solvents with two new promising candidates, namely *N*,*N*-dimethylformamide (DMF) and 1-methyl-2-pyrrolidone (NMP), which are polar aprotic solvents sharing similar properties to DMSO but that have not been explored as solvents for CuSCN so far. The observed solution colors provide a visible indication of oxidation and solvation state differences for the Cu metal sites. The resulting surface roughness for spin-coated thin films is also characterized. Next, the polymorphism found in drop-cast thick films is investigated, and X-ray photoelectron spectroscopy (XPS) is used to analyze the chemical composition and bonding for the spin-coated thin films. In addition, CuSCN surface energy is studied, playing an important role in tuning the ordering of polymer semiconductors deposited atop the interlayer and thereby influencing their charge carrier mobility. The IP values of the different CuSCN interlayers, which modulate hole injection barriers, are also characterized and discussed. Finally, device tests on selected OLEDs, OSCs, and OFETs are carried out, and their performance when using various CuSCN interlayers is referenced to devices with a PEDOT:PSS interlayer or simply no interlayer.

2. Solutions and Thin Films

CuSCN was dissolved in six solvents, namely DES, DPS, NH_4OH, DMSO, DMF, and NMP; details of these solvents and the conditions used for dissolution can be found in Table S1 (Supporting Information) and in the Experimental Section. The CuSCN concentration was 10 mg mL^{-1} for DES, DPS, NH_4OH, and DMSO solutions, whereas the saturated DMF and NMP solution concentrations were 2.1 and 2.8 mg mL^{-1}, respectively (see the Experimental Section for details). According to Pearson's Hard and Soft Acids and Bases theory,[28] Cu^+ as a soft

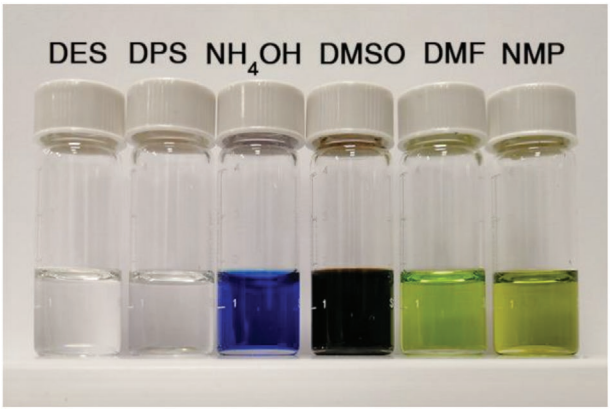

Figure 1. Photograph of CuSCN solutions evidencing the strong color changes for different solvents, indicative of changing ionic states and complex formation. The concentration is 10 mg mL^{-1} for the first four, and 2.1 and 2.8 mg mL^{-1} for DMF and NMP solutions, respectively, which are the saturation concentrations at room temperature.

acid interacts more easily with soft bases, which is the case for sulfur-containing DES, DPS, and DMSO. In comparison, the inclusion of nitrogen atoms in DMF and NMP makes them much "harder", leading to reduced solubility (Table S1, Supporting Information). An exception here is NH_4OH, which is a hard base but can dissolve CuSCN readily. This may be related to the quick oxidation of Cu^+ in the presence of NH_4OH (see discussion below), with the product Cu^{2+} a much "harder" acid.[29] **Figure 1** shows a photograph of typical solutions; the DES and DPS solutions are colorless, while the NH_4OH solution is deep blue, all in line with previous reports.[27d] A dark brown solution is obtained when DMSO is used as the solvent, and DMF and NMP solutions are light green and greenish yellow, respectively.

When CuSCN is dissolved, the solvent molecules can form complexes with Cu^+ and thereby break or weaken the ionic bond to SCN^-.[25] The color differences give an indication of the changes in chemical state and bonding of the copper in these solutions. For example, Cu(I)–amine complexes are generally colorless,[30] so the deep blue CuSCN–NH_4OH solution is likely caused by at least partial formation of a [Cu(II)–amine]$^{2+}$ complex ion. This oxidation is confirmed by XPS analysis (see Section 4). The colors of Cu(I) complexes are very dependent on their organic ligands;[30] the similar colors for DMF and NMP solutions then suggest that the copper is present in a broadly similar chemical environment, as might be expected from the similarity of the DMF and NMP chemical structures (Table S1, Supporting Information). By contrast, the very different color of the CuSCN in DMSO solution indicates different coordination in the presence of the sulfoxide moiety.

The solutions were spin-coated on ITO-coated glass substrates, the most commonly used transparent electrode

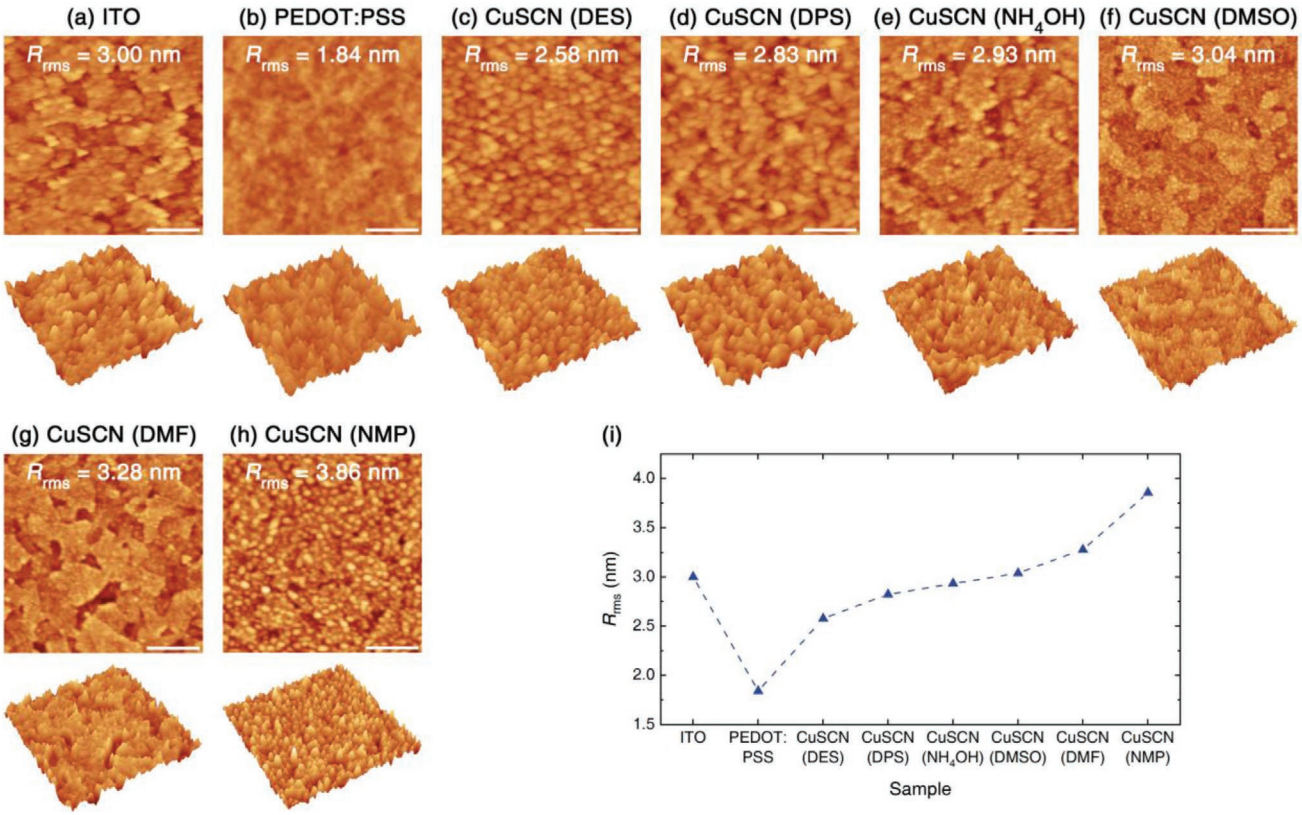

Figure 2. AFM images and deduced roughnesses for ITO and interlayer-coated ITO substrates. a–h) 2D (upper panels) and 3D (lower panels) topographies for: a) bare ITO; b) ITO/PEDOT:PSS; c) ITO/CuSCN (from DES solution); d) ITO/CuSCN (DPS solution); e) ITO/CuSCN (NH_4OH solution); f) ITO/CuSCN (DMSO solution); g) ITO/CuSCN (DMF solution); and h) ITO/CuSCN (NMP solution). The scale bars in each 2D image represent 500 nm. The root-mean-square roughness (R_{rms}) values are collected together in (i) for all samples. The dashed line is a guide to the eye.

in organic electronic devices, to form CuSCN thin films, and atomic force microscopy (AFM) was applied to characterize surface topography and roughness in an area of 2×2 μm^2 (**Figure 2**). Here we also include the results of bare ITO and ITO/PEDOT:PSS as references. Figure 2a for the bare ITO substrate reveals the characteristic polycrystalline grain microstructure[15a,27d] with grain sizes of several hundred nanometers; the root-mean-square roughness (R_{rms}) is 3.00 nm. When coated with PEDOT:PSS (Figure 2b), the substrate becomes smoother (R_{rms} = 1.84 nm), one of the well-documented benefits of the PEDOT:PSS HTL.[15,27d] CuSCN thin films processed from DES and DPS solutions comprise ≈50 nm crystalline grains (Figure 2c,d) with R_{rms} = 2.58 and 2.83 nm, respectively, somewhat smoother than for bare ITO but rougher than when PEDOT:PSS is used. In earlier publications, thicker CuSCN-DES and CuSCN-DPS films (around 50 nm) have been reported to have a higher R_{rms} than ITO.[15b,27d] In this study, all CuSCN films were controlled to be ≈10 nm thickness (see the Experimental Section) in order to be able to compare the six solvents side by side; the limited solubility of CuSCN in DMF and NMP precludes the straightforward preparation of spin-coated thicker films.

The CuSCN thin film microstructure resulting from NH_4OH, DMSO, and DMF solutions is similar to that of bare ITO (Figure 2e–g), possibly due to the thinness of the films and the lack of significant crystalline grain formation. The R_{rms} for these three samples is also close to that of ITO. Finally, for the CuSCN-NMP film (Figure 2h), a much rougher surface with R_{rms} = 3.86 nm is observed, and its topological characters differ a lot from the CuSCN-DMF sample. Considering the similarity in chemical structure between these two solvents, we propose that during spin-coating, the higher boiling point of NMP (203 °C) makes it slower to evaporate, facilitating crystallization and leading to a rougher surface. Figure 2i summarizes the R_{rms} values for all eight surfaces, among which PEDOT:PSS shows the best smoothing effect. For all bar the NMP-processed, the CuSCN thin films show a similar surface roughness to that of ITO; in the latter case R_{rms} is ≈30% larger.

3. Polymorphism

Crystalline CuSCN can exhibit at least two polymorphs, namely α- and β-CuSCN. The former has an orthorhombic crystal lattice,[31] while the latter can be either rhombohedral (the 3R polytype) or hexagonal (the 2H polytype).[32] Density functional theory (DFT) calculations show that the unit cell of β-CuSCN has ≈60 meV lower energy than that of the α-phase,[33] confirming β-CuSCN to be thermodynamically the most stable polymorph. This is consistent with previous reports that β-CuSCN films are commonly obtained by drop-casting,[26a] electrodeposition,[34] and successive ionic layer adsorption and reaction (SILAR),[35] whereas α-CuSCN films can only be achieved under some nonequilibrium conditions, for example during electrodeposition in the presence of selected organic additives.[36] Other polymorphs, e.g., γ, δ, and ε-CuSCN, have been predicted by DFT calculations[37] yet not been experimentally observed.

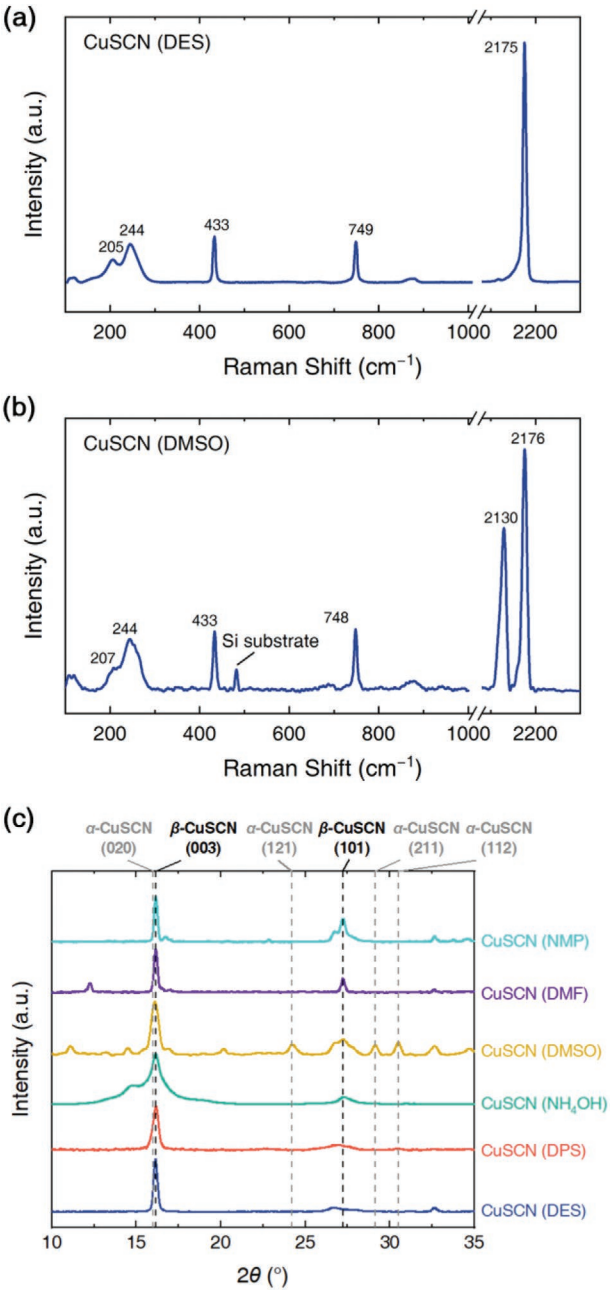

Figure 3. Raman and XRD characterization of the polymorphism in CuSCN thick films drop-cast from different solvents. a,b) Raman spectra excited at 532 nm for CuSCN samples processed from DES and DMSO solutions, respectively. Spectra of other samples are shown in Figure S1 in the Supporting Information. c) XRD patterns of CuSCN layers processed from DES, DPS, NH_4OH, DMSO, DMF, and NMP (from bottom to top). Characteristic diffraction peaks for α- and β-CuSCN are indicated.

We performed Raman spectroscopy and X-ray diffraction (XRD) measurements on drop-cast CuSCN films deposited from each of the solvents in order to investigate their polymorphism. Drop-cast films (see the Experimental Section for details) are needed to provide a sufficient X-ray scattering volume for crystallographic structure determination. **Figure 3**a,b shows the 532 nm laser excitation Raman spectra for CuSCN films

drop-cast from DES and DMSO solutions, respectively. Similar peaks are observed for both samples at lower Raman shift, i.e., ≈205 cm^{-1} for Cu–S stretching, 244 cm^{-1} for Cu–N stretching, 433 cm^{-1} for S–C≡N scissoring, and ≈749 cm^{-1} for C–S stretching.[38] However at higher Raman shift, the CuSCN-DES deposited sample shows a single peak at 2175 cm^{-1} corresponding to C≡N stretching in β-CuSCN[32,38b] while the CuSCN-DMSO film has an additional peak at 2130 cm^{-1}. The latter can be assigned to C≡N stretching in α-CuSCN,[32,38b] demonstrating that with DMSO as solvent, drop-cast films contain both α- and β-CuSCN polymorphs. The intensity of these two peaks can be used to estimate the ratio of α- to β-phase, which turns out to be 0.67:1. All other samples show Raman spectra that are similar to the CuSCN-DES case (Figure S1, Supporting Information), consistent with a purely β-CuSCN crystal structure. Fourier-transform infrared (FTIR) spectra (Figure S2, Supporting Information) complement the Raman data and confirm this conclusion.

The polymorphism of various CuSCN films is further confirmed by XRD patterns (Figure 3c). While all samples exhibit (003) and (101) peaks of the β-phase (the Powder Diffraction File, PDF 29-0581), the one processed from DMSO additionally shows (121), (211), and (112) α-phase peaks (PDF 29–0582).[39] From the relative intensity of the α-phase (112) and β-phase (101) peaks and considering the observed difference in scattering cross sections (0.80:0.75 from the PDF), the ratio of the two polymorphs is calculated to be 0.74:1, in reasonable agreement with the estimation from Raman results. The coexistence of both polymorphs was previously observed in a 14 nm thick CuSCN film processed from DPS solution, characterized by transmission electron microscopy (TEM) and selected area electron diffraction (SAED).[40] For our CuSCN-DMSO sample, the way Cu(I) coordinates with DMSO molecules may affect the crystallization process, leading to a mixture of the most stable and metastable phases; the detailed mechanism still remains open and is an interesting topic for future research. Nonetheless, this finding provides a useful platform with which the relationship between CuSCN polymorphs and electronic properties can be experimentally investigated, complementing previous theoretical studies.[33] We note the caveat, however, that the samples used here for X-ray diffraction are several micrometers in thickness, whereas thin films of ≈10 nm are used in the devices reported below. How much the variation in thickness and associated processing conditions lead to a variation in polymorphism remains unclear. The suggestion, though, is that depositing films from DMSO is likely to be a more complex process.

4. Surface Chemistry

The surface chemistry features of CuSCN films on fused silica substrates were investigated by XPS and unlike the thick layers used in Raman and XRD measurements, these measurements used spin-coated thin films (see the Experimental Section), just as used in devices (Section 7). Survey spectra (Figure S3, Supporting Information) confirm the existence of Cu, S, C, and N in all samples, with Si and O signals also seen from the substrates. High-resolution C 1s core level spectra (Figure S4, Supporting Information) for all samples show, as expected, peaks associated with S–C≡N at ≈286.4 eV and adventitious carbon at 284.8 eV.[26a,27d] Traces of residual solvent are also observed, namely C–S peaks for DES-, DPS-, and DMSO-processed samples and C–N peaks for DMF- and NMP-processed. The case of NH_4OH will be discussed separately below; N 1s spectra are needed since there is no C present in the solvent. It has been reported that DES and DPS molecules are easily trapped inside the CuSCN thin film, even after annealing at temperatures higher than their boiling points, due to the strong coordination between Cu(I) and di-alkyl sulfides.[41] In terms of DMSO, DMF, and NMP, their high boiling points (Table S1, Supporting Information) may additionally hinder their removal during thermal annealing. Finally, C=O peaks at ≈288.5 eV[42] are also observed for the samples processed from NH_4OH, DMSO, DMF, and NMP, indicating the presence of adventitious oxidation products.

The N 1s core level spectra of all samples (Figure S4, Supporting Information) show a characteristic S–C≡N peak at ≈398.9 eV, consistent with previous reports.[27d,40] Additional N–H peaks at 400.2 eV in DES- and DPS-processed thin films, as observed before,[27d] can be attributed to partial protonation of some of the nitrogen atoms. A much stronger N–H peak is seen for NH_4OH-processed samples, probably stemming from solvent residues bound to CuSCN.[27d] C–N peaks appear at ≈399.9 eV for DMF- and NMP-processed samples, confirming the evidence from the C 1s spectra that there is some residual solvent present.

Figure 4 presents the S 2p core level spectra, with S–C≡N evident for all samples, located at ≈163.8 eV for S $2p_{3/2}$.[43] Thin films processed from DES and DPS exhibit C–S peaks around 163.6 eV ($2p_{3/2}$),[44] again arising from residual solvent molecules. These two samples further show very weak S–O peaks at ≈169.6 eV ($2p_{3/2}$), suggesting a marginal degree of oxidation of sulfur, as reported previously.[27d] This oxidation is more pronounced in the last four samples (Figure 4c–f) and may lead to a shift in the CuSCN valence band edge due to a change in the configuration of the outermost electrons, as predicted by DFT calculations.[26a] The oxidation process may result in sulfate ions SO_4^{2-} being formed, producing S vacancies in the CuSCN lattice. However, this type of defect has been shown to be electrically inactive.[26a]

High-resolution spectra of Cu 2p core levels are displayed in **Figure 5**. While all samples show Cu^+ peaks at ≈933.0 eV,[26a,27d] thin films processed from NH_4OH, DMSO, DMF, and NMP exhibit an additional peak at ≈934.6 eV, which can be assigned to Cu^{2+}.[45] This is further corroborated by the characteristic Cu^{2+} satellite peaks around 943 eV.[46] Similar to the case of sulfur, the partial oxidation of Cu^+ can affect the position of CuSCN valence band edges in the last four samples through the change in 3d electrons.[26a] Moreover, the oxidation product, Cu^{2+} ions, may act as p-dopants to CuSCN if Cu^{2+} can replace Cu^+ in the lattice, or lead to Cu vacancies if Cu^{2+} cannot. In the latter case, Cu^{2+} ions are likely to exist in the form of Cu^{2+}–amine complexes (for NH_4OH-processed) or $CuSO_4$ (for DMSO-, DMF-, and NMP-processed). Both possibilities can cause a shift in the CuSCN Fermi level, and will be discussed further in Section 6.

Finally, we measured the O 1s core level spectra (Figure S6, Supporting Information). Oxygen is not expected to appear

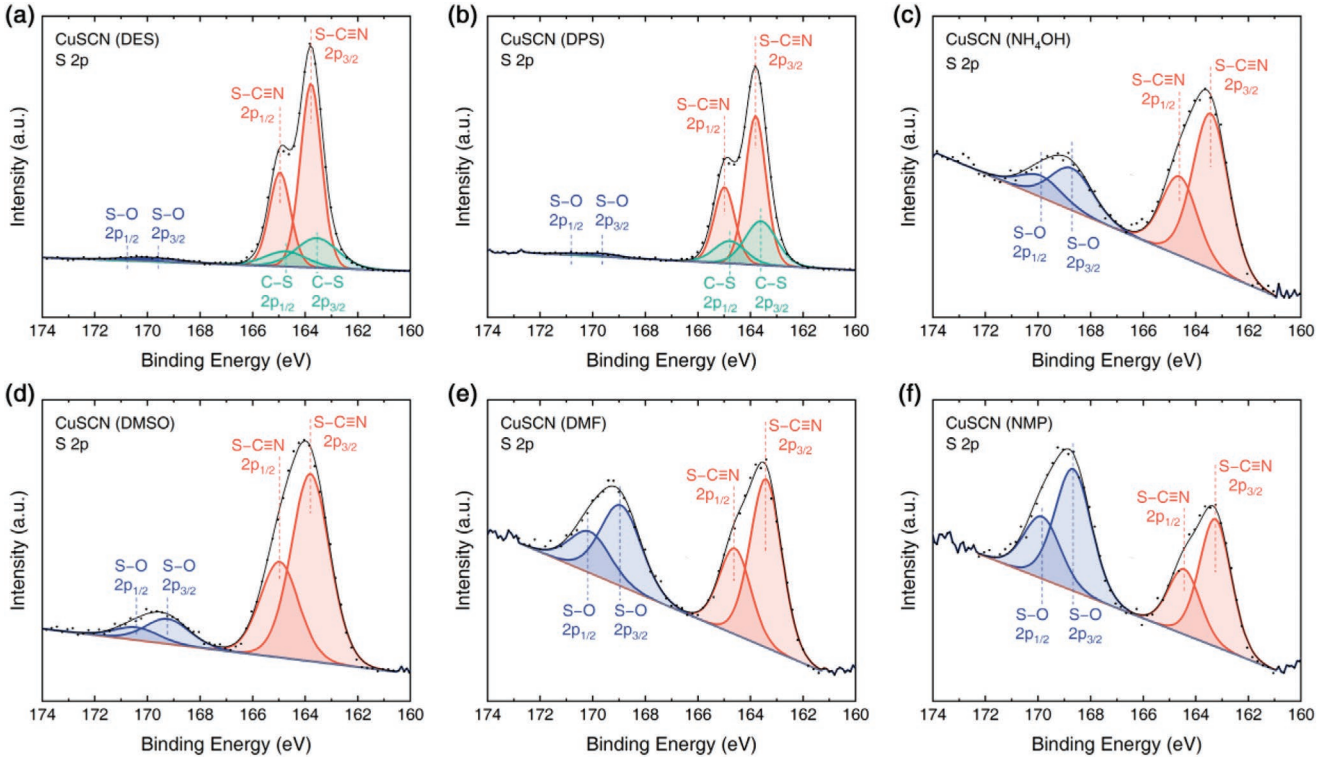

Figure 4. XPS high-resolution spectra of S 2p core level for CuSCN thin films processed from a) DES, b) DPS, c) NH_4OH, d) DMSO, e) DMF, and f) NMP solutions. Data points are shown by black dots, and the envelopes from the peak fitting analysis are shown by black curves. Fitted peaks and assigned chemical bonds are color coded: S–C≡N (red), S–O (blue), and C–S (green).

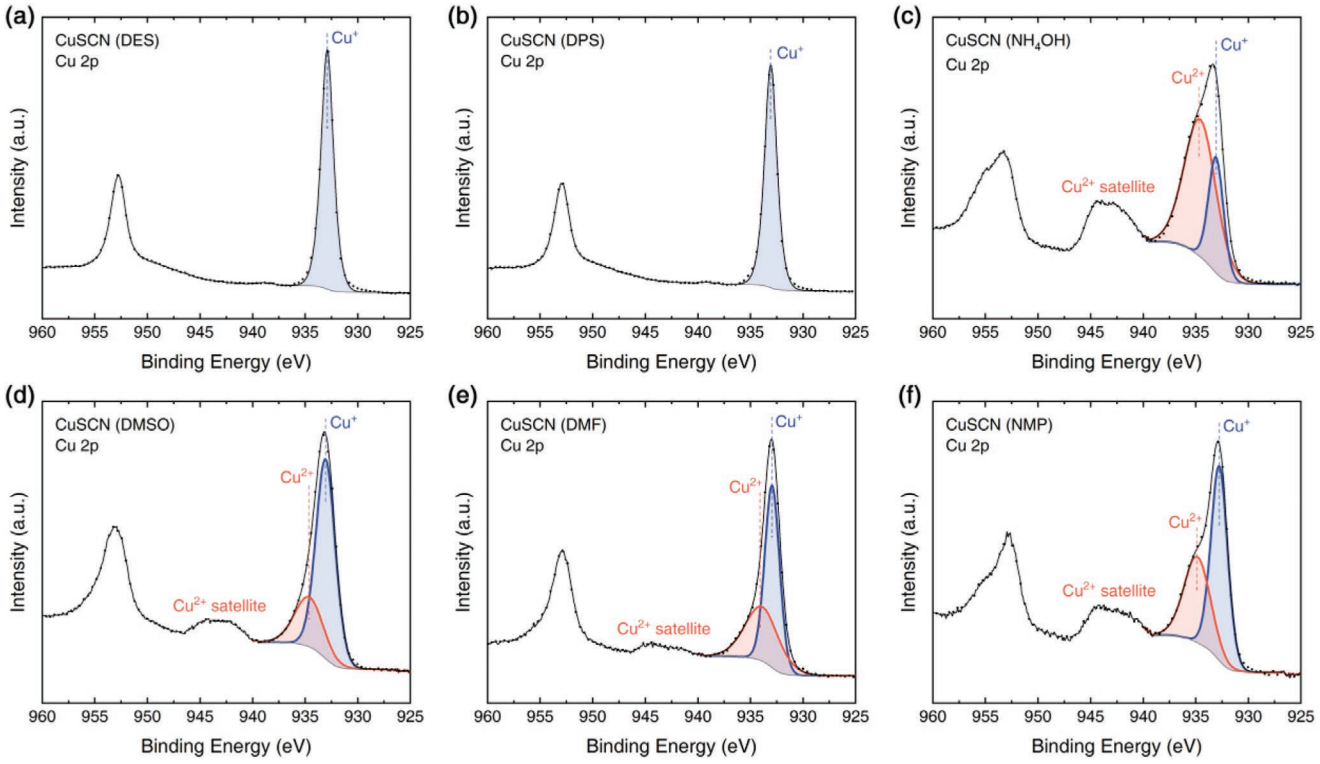

Figure 5. XPS high-resolution spectra of Cu 2p core level for CuSCN thin films processed from a) DES, b) DPS, c) NH_4OH, d) DMSO, e) DMF, and f) NMP solutions. Data points are shown by black dots, and the envelopes from the peak fitting analysis are shown by black curves. Fitted peaks and assigned Cu chemical states are color coded: Cu^+ (blue) and Cu^{2+} (red).

in pure CuSCN thin films; however, oxidation products, the adsorption of moisture, and the background signal from the fused silica substrates can all contribute. These sources lead to C=O, S–O, O–H, and Si–O peaks for various samples. Interestingly, in CuSCN-DMSO thin films, there is a peak at 530.2 eV, which possibly originates from the existence of Cu_2O.[47] The latter has a smaller IP (≈5.3 eV)[48] than CuSCN and has been used as a hole injection/transport material in its own right. A mixture of both may result in a cascaded hole injection/extraction interface, provided that a favorable composition gradient can be formed normal to the film plane. Such a Cu_2O/CuSCN composite HTL has already been used in perovskite solar cells to enhance charge transport and inhibit interfacial degradation,[49] but with different processing methods from us. Therefore, further investigations are needed to explore the origin and applications of this effect. By and large, the CuSCN thin films studied here exhibit some complexity in the chemistry related to the different processing solvents, leading to a variation in the chemical composition and bonding of the resulting films, with, as already noted, the DMSO-processed films being the most complicated.

5. Surface Energy, Polymer Orientation, and Mobility

In addition to the chemical composition of the interlayer surface, its surface energy will have an impact on the orientation of a semicrystalline conjugated polymer spin-coated on top, influencing the charge transport properties.[50] Specifically, interlayers with low surface energies tend to favor "edge-on" orientation of the polymer, while "face-on" orientation is often promoted when surface energies of interlayers increase.[51] For diode structures where charge carriers flow in the normal-to-plane direction, face-on oriented chain packing is beneficial for charge transport.[50] We have, therefore, examined the surface energy of the interlayers processed from the six different solvents and their ability to tune the orientation and mobility of a widely studied polymer semiconductor, poly[[4,8-bis[(2-ethylhexyl)oxy]benzo[1,2-*b*:4,5-*b*′]dithiophene-2,6-diyl][3-fluoro-2-[(2-ethylhexyl)carbonyl]thieno[3,4-*b*]thiophenediyl]] (PTB7, see **Figure 6**d).[52]

The surface energies of the CuSCN thin films deposited from the six solvents were investigated in the framework of Fowkes theory,[53] assuming that the surface energy γ_S can be described in terms of two components, namely a dispersive (nonpolar) component γ_S^D and a polar component γ_S^P. The surface tension of a liquid γ_L is likewise represented via a dispersive part γ_L^D and a polar part γ_L^P, and the contact angle, θ, for the liquid on the surface is expected to be given by[54]

$$\sqrt{\gamma_S^D \gamma_L^D} + \sqrt{\gamma_S^P \gamma_L^P} = \frac{\gamma_L(1+\cos\theta)}{2} \quad (1)$$

The γ_S for CuSCN thin films can then be extracted using the contact angles obtained from two different liquids with known surface tension components.[55] Figure 6a shows contact angle measurements for deionized (DI) water (upper panels) and diiodomethane (DIM, lower panels) droplets sitting on a CuSCN-DES thin film; results for other CuSCN interlayers are shown in Figure S7 in the Supporting Information. The calculated surface energies are presented in Figure 6e by gray bars, of which the lower parts (in deeper gray) and the upper parts (in lighter gray) indicate the dispersive and polar components, respectively. All CuSCN thin films are found to have similar dispersive surface energies around 50 mJ m^{-2}, yet samples processed from NH_4OH, DMSO, DMF, and NMP solutions show significantly higher polar surface energies (≈25 mJ m^{-2}) than those from DES and DPS solutions (≈10 mJ m^{-2}), leading to higher total surface energies of the former group. DFT calculations revealed that for β-CuSCN, polar surfaces such as (101) and (001) have higher energies than the nonpolar, e.g. (110) and (100), leading to an expectation of low polarity surfaces under equilibrium growth.[56] Hence, the different surface energies for CuSCN thin films may result from nonequilibrium processes yielding different surface orientations, affected by both the nature of Cu(I)-solvent molecular complexes in solution and the kinetics of layer deposition. Further work will be needed to understand the degree to which the CuSCN surface orientation can be controlled and its long-term microstructural stability.

PTB7 (Figure 6d) was spin-coated on top of CuSCN interlayers deposited from each of the six solvents to investigate the influence of surface energy on polymer orientation. For this purpose, grazing-incidence wide-angle X-ray scattering (GIWAXS) patterns were collected for all CuSCN/PTB7 samples (Figure S8, Supporting Information); the result for CuSCN-DES/PTB7 is shown in Figure 6b as an example. The peaks at $q_{xy} \approx 0.38$ Å^{-1} and $q_z \approx 1.6$ Å^{-1} correspond to face-on oriented PTB7 crystallites, while the peak at $q_z \approx 0.38$ Å^{-1} signals the presence of edge-on orientation.[57] Note that the peak at $q_{xy} \approx 1.2$ Å^{-1} is from the CuSCN layer underneath. In order to quantitatively compare the face-on content, we calculated the intensity ratio of the $q_{xy} \approx 0.38$ Å^{-1} peak (face-on) to the $q_z \approx 0.38$ Å^{-1} peak (edge-on). These values are plotted in Figure 6e as red dots. Use of NH_4OH, DMSO, DMF, and NMP as CuSCN solvent allows a higher fraction of face-on orientation for the PTB7 semiconductor layer, showing a positive correlation with interlayer surface energy, consistent with previous reports.[50–51]

To test the influence of face-on orientation on charge transport in diode structures, we fabricated metal–insulator–semiconductor structures for charge carrier extraction by linearly increasing voltage (MIS-CELIV) measurements.[58] MIS-CELIV is a variant of the better known standard CELIV measurement that can selectively determine hole or electron mobility due to the unipolar nature of the MIS diode. Here hole-only devices were fabricated so that, after injection, holes accumulate at the semiconductor–insulator interface. A linearly increasing voltage is then applied to extract the injected holes, and a transient current density trace for hole transport can be obtained. The hole mobility μ is given by[59]

$$\mu = \frac{\pi^2 d_s^2}{8 A t_{2j_0}^2}\left(1 + \frac{\varepsilon_s d_i}{\varepsilon_i d_s}\right) \quad (2)$$

where d_s (d_i) is the thickness of the semiconductor (insulator) layer, ε_s (ε_i) is the permittivity of the semiconductor (insulator), A is the slope of the linearly increasing voltage (in V s^{-1}), and t_{2j_0} is the time for the current density to rise to twice the displacement current density j_0. The measured transient

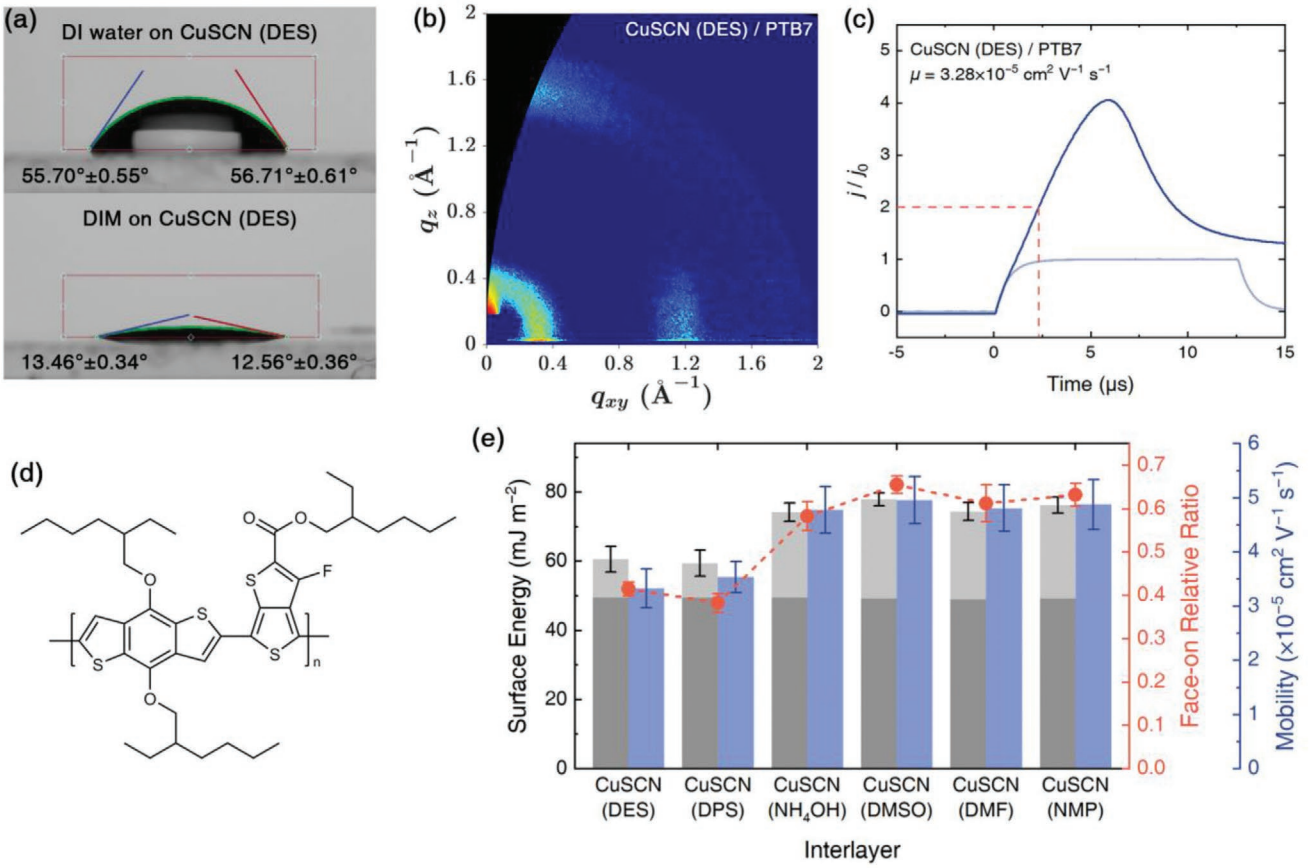

Figure 6. Surface energy measurements for CuSCN thin films, and orientation and mobility of PTB7 layers deposited on top. a) Contact angles for deionized (DI) water (upper panel) and diiodomethane (DIM, lower panel) on a CuSCN thin film processed from DES solution. Contact angle measurements for other CuSCN samples are shown in Figure S7 in the Supporting Information. b) GIWAXS pattern of PTB7 spin-coated on top of a CuSCN-DES interlayer. Figure S8 in the Supporting Information contains PTB7 GIWAXS patterns for CuSCN interlayers processed from the other five solvents. c) MIS-CELIV hole mobility measurements for PTB7 deposited on a CuSCN-DES interlayer. Current density transients with (blue upper curve) and without (faint blue lower curve) hole injection are shown; the red dashed lines highlight the time at which $j = 2j_0$. The MIS-CELIV results for PTB7 deposited on the other CuSCN interlayers are shown in Figure S9 in the Supporting information. d) Chemical structure of PTB7. e) Summary of the variation in CuSCN surface energy (gray bars), PTB7 orientation (red dots), and PTB7 mobility (blue bars) as a function of the solvent used to deposit the films. The deep gray (lower) and light gray (upper) parts represent the dispersive and polar surface energies, respectively. The dashed red line connecting the orientation data is a guide to the eye.

current density characteristics for a CuSCN-DES/PTB7 sample are shown in Figure 6c, yielding PTB7 hole mobility $\mu = 3.28 \times 10^{-5}$ cm^2 V^{-1} s^{-1}, slightly lower than previously reported values of ≈10^{-4} cm^2 V^{-1} s^{-1}.[57,60] We note that such differences are not unusual when using different sample processing methods,[60] different device architectures and different mobility measurement techniques (space-charge-limited current[57,60] versus MIS-CELIV). Results for PTB7 deposited on top of the other five CuSCN interlayers can be found in Figure S9 in the Supporting Information, and the extracted mobility values (from more than 10 devices for each interlayer) are shown by the blue bars in Figure 6e. The higher face-on fraction for PTB7 on NH_4OH-, DMSO-, DMF-, and NMP-processed CuSCN interlayers leads to an increased normal-to-plane hole mobility of about 5×10^{-5} cm^2 V^{-1} s^{-1}, compared with ≈3×10^{-5} cm^2 V^{-1} s^{-1} for DES- and DPS-processed, i.e., an improvement by ≈40%.

These results confirm that the choice of CuSCN interlayer solvent can significantly affect the charge transport properties of a p-type semicrystalline conjugated polymer overlayer via the resulting differences in surface energy and their influence on polymer crystallite orientation. NH_4OH, DMSO, DMF, and NMP are better choices than conventional DES and DPS to achieve improved diode-relevant, normal-to-plane mobility.

6. Energy Levels and Hole Injection

We next turn to the hole-injection properties of the differently processed CuSCN interlayers, which should primarily be determined by their energy levels. To this end, air photoemission spectroscopy (APS) was used to measure the IPs that result from deposition using the six different solvents.[61] Based on the photoelectric effect, this technique records the number of photoelectrons escaping from the surface when monochromatic light of varying energy is incident on the sample. According to Fowler's analysis of photoemission, the onset energy in a plot of the cube root of the photoelectron yield versus incident light energy marks the IP value of a semiconductor.[62] Compared

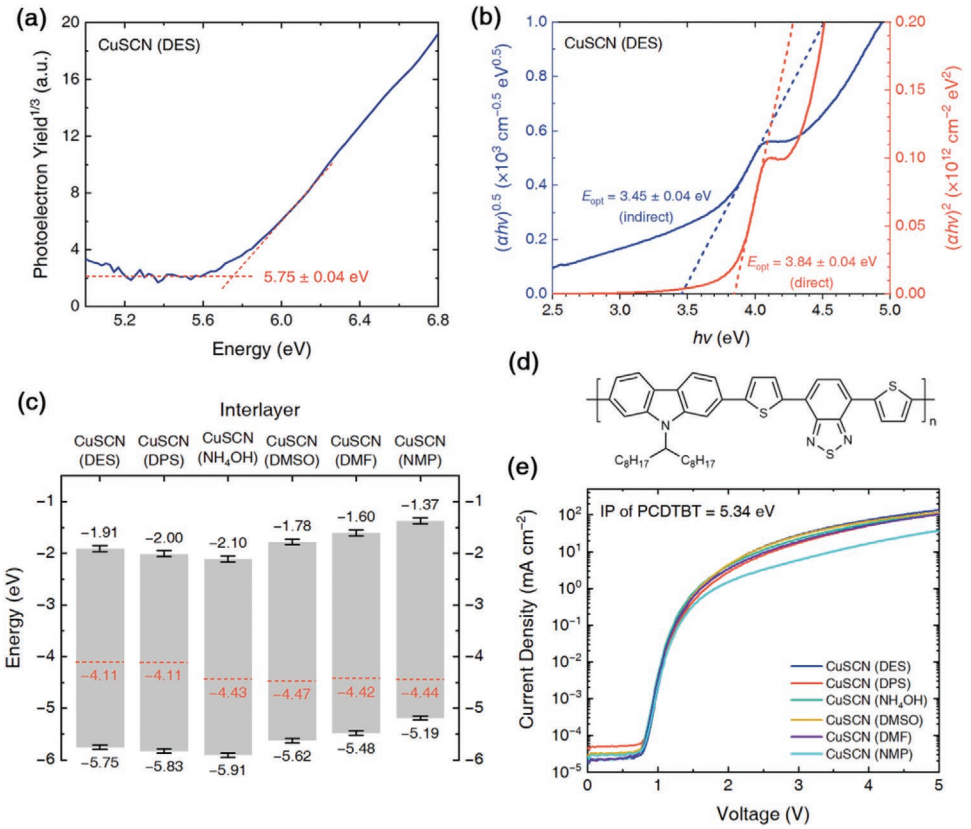

Figure 7. Energy levels and *J–V* characteristics for CuSCN interlayers processed from six different solvents. a) APS results for a CuSCN-DES thin film, detailing extraction of the IP value. APS spectra of the other CuSCN interlayers are shown in Figure S10 in the Supporting Information. b) Tauc plots derived from the absorbance spectrum of CuSCN-DES thin film. Both $(\alpha h\nu)^{0.5}$ and $(\alpha h\nu)^2$ are plotted, corresponding to the expectation for indirect (blue) and direct (red) band gaps, respectively. Tauc analysis of other CuSCN thin films can be found in Figure S11 in the Supporting Information. c) Energy level diagram for the various CuSCN interlayers. Band gaps (gray bars) are assumed to be direct. Red dashed lines represent WFs measured by Kelvin probe, the uncertainties for which are small and therefore not shown (Figure S12, Supporting Information). d) Chemical structure of PCDTBT. e) Forward bias *J–V* characteristics for PCDTBT diodes using differently processed CuSCN interlayers, from which holes are injected into the polymer; all interlayer films are ≈10 nm thickness.

with commonly used ultraviolet photoemission spectroscopy (UPS) which requires a high vacuum, APS is performed in an ambient environment, closer to real device fabrication conditions. **Figure 7**a presents the APS results for a CuSCN thin film processed from DES solution; the IP value is determined to be 5.75 ± 0.04 eV. APS measurement results for the other CuSCN interlayers are shown in Figure S10 in the Supporting Information.

In addition, the optical gaps (E_{opt}) of different CuSCN thin films were extracted from their absorbance spectra via Tauc plots.[63] Both direct and indirect band gap models can be fitted by plotting $(\alpha h\nu)^2$ and $(\alpha h\nu)^{0.5}$, respectively, versus photon energy, $h\nu$, where α is the absorption coefficient (in cm^{-1}). Figure 7b provides an example of the Tauc analysis performed for a CuSCN-DES thin film; 3.84 ± 0.04 and 3.45 ± 0.04 eV direct and indirect band gap energies, respectively, are obtained. Results for other CuSCN interlayers can be found in Figure S11 in the Supporting Information. We note that the nature of the CuSCN band gap is still under debate,[26b] and that is why we analyze the same dataset of CuSCN absorbance using both models. In the literature, although DFT calculations predict CuSCN band gap to be indirect,[26a] most experimental values are around 3.8 eV, consistent with the calculated value of a direct band gap.[26,43] This discrepancy may be related to a very small oscillator strength for the lowest indirect transition, as this process requires phonons to assist.[26a] For our measurements, it can be clearly seen from Figure 7b that the presumption of a direct band gap (red) is more reasonable, since for the indirect (blue), the characteristic parameter $(\alpha h\nu)^{0.5}$ does not cut off at the nominal "band gap." Also, the extracted direct band gap values are very consistent for different CuSCN samples, in contrast with the scattered values obtained from the indirect gap model (Figure S11, Supporting Information). Nonetheless, these results are not unambiguous evidence for a direct band gap of CuSCN due to the >0.5 eV absorption tail below the determined direct gaps rather than an abrupt cutoff. Possible reasons for the absorption tail include weak indirect transitions at lower energies, an amorphous fraction, polymorphism, or a combination of these factors.[26] Therefore, this topic still needs further elucidation, but what is for sure is that the band gap, irrelevant of its nature, is sufficiently wide (≥3.80 eV) for CuSCN interlayers to absorb very little in the visible spectral range.

For inorganic semiconductors, their high permittivity and consequently small exciton binding energy (usually a few meV)

allow us to approximate the electrical gap (E_g) to E_{opt}.[64] With this assumption, we can calculate electron affinities (EAs) for the CuSCN interlayers as EA = IP − E_{opt}, enabling us to establish a full energy level diagram for the CuSCN thin films processed from different solvents, as shown in Figure 7c. The EA values span a wide range from 1.37 to 2.10 eV but for all samples are conducive to effective electron blocking. The IP values similarly span a wide range from 5.19 eV for the NMP-processed thin film to 5.91 eV for the NH_4OH-processed. Previous DFT calculations indicated that the position of the CuSCN valence band edge is mainly affected by the Cu 3d states, with a small contribution from S 3p hybridization.[26a] As shown in the XPS spectra of S 2p (Figure 4) and Cu 2p (Figure 5) core levels, the six CuSCN thin films do differ in the chemical states of these two elements, resulting in their different outermost (3d for Cu ions and 3p for S) electron configurations and consequently, different IPs for CuSCN interlayers. However, the detailed mechanisms behind this may require further theoretical input to clarify.

The WFs for films deposited from all six solvents were determined using Kelvin probe measurements (Figure S12, Supporting Information),[65] and the results are displayed in Figure 7c by red dashed lines. The WF values for CuSCN interlayers processed from DES and DPS are 4.11 eV, whereas for the other four they are around 4.45 eV, indicating Fermi levels lying deeper than the band gap center energy for all samples. For DES- and DPS-processed films, this can be understood from CuSCN being an intrinsic p-type semiconductor with a higher electron than hole effective mass.[26,40] For the other four, whose Fermi levels are much closer to their valence band edges, we attribute this, in addition to the intrinsic p-conductivity of CuSCN, to extrinsic p-doping. As mentioned in Section 4 in relation to the XPS spectra of Cu 2p core levels (Figure 5), the partial oxidation of Cu^+ to Cu^{2+} can result in either Cu^{2+} acting as a p-dopant or the introduction of Cu vacancies in the CuSCN lattice. It has been demonstrated that the latter vacancy defect/nonstoichiometry can contribute to an increased hole concentration in CuSCN by creating shallow acceptor levels,[26,33] leading to a similar effect on the Fermi level to that of p-doping. We infer, as a consequence, that it is the partial oxidation of Cu^+ in NH_4OH-, DMSO-, DMF-, and NMP-processed CuSCN thin films which leads to a further lowering of the Fermi level.

While IP values are a good indicator of the expected hole-injection properties of interlayers, other processes are known to play a role. These include the formation of interface dipoles, charge transfer across the interface, and specific chemical reactions.[5,66] To further compare the hole-injection properties of different CuSCN interlayers in real devices, we fabricated hole-only diodes using poly[*N*-9′-heptadecanyl-2,7-carbazole-*alt*-5,5-(4′,7′-di-2-thienyl-2′,1′,3′-benzothiadiazole)] (PCDTBT; Figure 7d), a polymer semiconductor with a suitable IP of 5.34 eV.[67] In the absence of any such complicating factors, from the deduced IP values, barrier-free hole injection into PCDTBT is expected for all of the CuSCN interlayers except for that processed from NMP solution where the IP value (5.19 ± 0.04 eV) is 0.15 eV smaller than the IP value (5.34 eV) for PCDTBT. The measured current density–voltage (*J*–*V*) characteristics (Figure 7e) are consistent with this anticipated situation; the curve for the CuSCN-NMP device shows a significantly lower current density for voltages above ≈1.5 V while all of the other curves align with each other.

To summarize this section, we have established a detailed picture of the variation in energy level structure for CuSCN interlayers processed from different solvents. The wide tuneability of CuSCN interlayer IP values from 5.19 to 5.91 eV opens an opportunity to minimize hole injection barriers for specific active materials by the careful selection of processing solvent.

7. Device Performance

Having investigated the optical and electrical properties of CuSCN interlayers processed from different solvents, we now report on their performance in representative OLED, OSC and OFET devices. Note that the CuSCN interlayer thickness was adjusted to be 8 ± 2 nm for all solvents, with four at ≈10 nm and two (processed from DMF and NMP) at ≈6 nm due to more limited solubility (see the Experimental Section for details). This ensures a relatively straightforward comparison of performance. First, simple OLED structures using the commercially available phenylene–vinylene copolymer Super Yellow (SY; Figure S13a in Supporting Information) as light-emitting material were fabricated. Comparison was made between PEDOT:PSS and a selection of CuSCN HILs/HTLs (see Figure S13b,c in the Supporting Information for device structure and nominal energy level diagram, respectively). Two figures of merit, namely the luminance (at 6 V) and maximum external quantum efficiency (EQE),[68] are reported for each of the devices in **Figure 8**a. All SY OLEDs share a similar maximum EQE of ≈3.5% but they differ in luminance, consistent with the difference in charge injection for different interlayers. In detail, the device using a CuSCN-DMSO interlayer has the highest luminance at 6 V (13 585 ± 1204 cd m^{-2}), significantly better than the reference device using PEDOT:PSS (10 264 ± 981 cd m^{-2}). In addition, when DES or DMF is used as solvent, a similar/somewhat higher luminance to that for the PEDOT:PSS-based device can be achieved. Previous research showed that for selected phosphorescent OLEDs, replacing PEDOT:PSS with DES-processed CuSCN retained comparable performance.[15a] Here we demonstrate that by choosing a specific solvent, namely DMSO in this case, it is possible to fabricate CuSCN-containing fluorescent polymer OLEDs that notably outperform PEDOT:PSS-containing devices with ≈32% higher luminance (at 6 V).

Inspired by the favorable polymer OLED performance, we next fabricated bulk-heterojunction OSCs using a blend of PTB7 and [6,6]-phenyl-C_{71}-butyric acid methyl ester ($PC_{71}BM$; Figure S14a, Supporting Information) as the active material. Again, comparison is made between CuSCN processed from different solvents and PEDOT:PSS (see Figure S14b,c in the Supporting Information for device structure and nominal energy level diagram, respectively). As shown in Figure 8b, a higher average power conversion efficiency (PCE) of ≈6.4% is achieved for the device using a CuSCN-DMSO interlayer, compared with the reference PEDOT:PSS device (≈5.8%). Prior reports have shown OSC efficiency improvement relative to PEDOT:PSS for CuSCN-DES[15b,27a] and CuSCN-NH_4OH[27d]

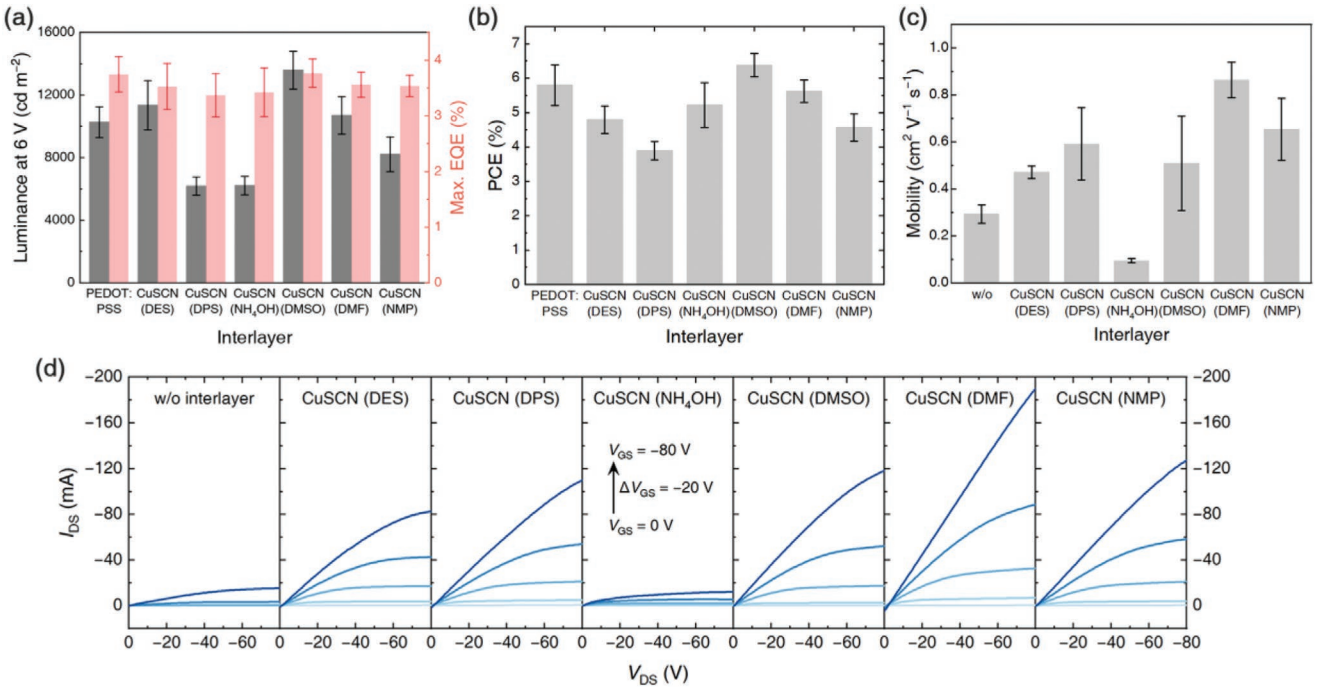

Figure 8. Performance of OLED, OSC and OFET devices using CuSCN interlayers processed from different solvents. a) Luminance (at 6 V) and maximum EQE values of SY polymer OLEDs. b) PCE of PTB7:$PC_{71}BM$ OSCs. c) PDPPTTT OFET hole mobility and d) output characteristics parametric in V_{GS} (from 0 to −80 V in −20 V steps). The device details are shown in Figures S13–S15 in the Supporting Information.

interlayers when using different active materials. It will be interesting, in future, to explore the optimization of different combinations of active materials and CuSCN films processed from different solvents for even better overall performance.

Finally, OFETs were fabricated using the high-mobility polymer, poly[[2,5-bis(2-octyldodecyl)-2,3,5,6-tetrahydro-3,6-dioxopyrrolo[3,4-*c*]pyrrole-1,4-diyl]-*alt*-[[2,2′-(2,5-thiophene) bis-thieno[3,2-b]thiophen]-5,5′-diyl]] (PDPPTTT; Figure S15a, Supporting Information). In these top-gate bottom-contact devices (Figure S15b, Supporting Information), CuSCN interlayers were inserted between the gold electrodes (as drain and source) and the polymer layer. Comparison in this case was referenced to uncoated Au electrodes. The hole mobility extracted from the linear regime (μ_{lin}) for all devices is shown in Figure 8c. The highest $\mu_{lin} = 0.86 \pm 0.07$ cm^2 V^{-1} s^{-1} is achieved for devices using a CuSCN-DMF interlayer, some three times higher than for the device with no interlayer (labeled w/o, with $\mu_{lin} = 0.29 \pm 0.04$ cm^2 V^{-1} s^{-1}). Five of the six solvents yield higher mobility than the reference device; CuSCN–NH_4OH is the exception. We note that CuSCN processed from NH_4OH solutions has also been used in transistors as a semiconducting layer rather than an interlayer, and showed higher hole mobility than for devices with a DES-processed CuSCN semiconducting layer.[27d] The output characteristics (Figure 8d) also clearly show the significant enhancement engendered by the CuSCN-DMF interlayer; the drain current I_{DS} at $V_{GS} = V_{DS} = -80$ V can reach ≈190 mA for these devices, compared to ≈20 mA when the interlayer is absent. The improved mobility and channel current are expected to be related to a better match between the CuSCN-modified electrode and PDPPTTT IP values. The latter was measured to be 5.3 eV (Figure S15c, Supporting Information),[69] with the CuSCN interlayer processed from DMF having the closest IP value (5.48 ± 0.04 eV; Figure 7c), greatly reducing the injection barrier between Au (WF = 4.9 eV)[70] and PDPPTTT.

To summarize this section, we successfully demonstrated that by choosing an appropriate CuSCN solvent, representative polymer OLEDs, OSCs, and OFETs with CuSCN interlayers can perform better than reference devices either with PEDOT:PSS interlayers or without an interlayer. DMSO and DMF solvents are found to allow the formation of CuSCN interlayers that facilitate better device performance than for the conventional but undesirable solvent choices of DES and DPS. While it is not straightforward to fully decouple the different factors (discussed above) that control this improved device performance, our device tests clearly indicate the opportunity for further progress through introduction of novel CuSCN solvents.

8. Conclusion

In this paper we report a comprehensive study on the properties and applications of CuSCN interlayers processed from six different solvents, namely DES, DPS, NH_4OH, DMSO, DMF, and NMP. In the case of DMSO, drop-cast thick films comprise a mixture of the α- and β-phase crystalline polymorphs whereas all other solvents yield films containing only β-CuSCN. Thin films deposited by spin-coating showed similar surface roughness, with R_{rms} values close to that of the underlying ITO-coated glass substrate (except for NMP-processed films that are ≈30% rougher). However, their chemical compositions differ; in samples processed from NH_4OH, DMSO, DMF, and NMP

solutions, there is a noticeable oxidation of sulfur, yielding S–O bonds, and copper to Cu^{2+}, with an associated impact on CuSCN electronic structure.

The solvent used to deposit CuSCN interlayers affects the hole injection and transport properties in two different ways. First, ordering of the semicrystalline conjugated polymer, PTB7, deposited on top of the CuSCN interlayers processed from the six solvents is influenced by their different surface energies. This leads to different PTB7 normal-to-plane hole mobilities, with ≈40% higher values of $\approx 5 \times 10^{-5}$ cm^2 V^{-1} s^{-1} when NH_4OH, DMSO, DMF, or NMP is used as the solvent. The higher surface energies of CuSCN thin films processed therefrom (≈75 mJ m^{-2}, compared with ≈60 mJ m^{-2} for DES- and DPS-processed) support a higher fraction of face-on oriented crystallites. Second, significantly different IP values ranging from 5.91 to 5.19 eV result for CuSCN interlayers processed from different solvents in the sequence NH_4OH > DPS > DES > DMSO > DMF > NMP, leading to different hole injection properties. This is confirmed by the *J–V* characteristics for hole-only diodes, demonstrating the possibility to minimize hole injection barriers by appropriate selection of CuSCN solvent to achieve a good match in IP values between CuSCN interlayers and active materials.

Finally, device tests show that in polymer OLEDs, OSCs, and OFETs, using CuSCN interlayers processed from suitable solvents can boost the performance compared with reference devices. In particular, for the devices studied in this work, the best performance is provided by DMSO and DMF, more benign solvents than the initially used DES and DPS. These results pave the way for a wider use of solution-processed CuSCN interlayers in a variety of organic electronic devices and expand the selection range for hole-injection/transport materials as alternatives to PEDOT:PSS.

9. Experimental Section

Materials: CuSCN (99%), diethyl sulfide (98%), dipropyl sulfide (97%), dimethyl sulfoxide (99.9% anhydrous), *N*,*N*-dimethylformamide (99.8% anhydrous), 1-methyl-2-pyrrolidinone (99.5% anhydrous), chlorobenzene (99.8% anhydrous), 1,2-dichlorobenzene (99% anhydrous), toluene (99.8% anhydrous), *n*-butyl acetate (99.5%), 1,8-diiodooctane (98%), super yellow polymer (M_n > 400000, M_w > 1300000), and poly(methyl methacrylate) (PMMA, M_w = 120000, polydispersity = 2.2) were obtained from Sigma-Aldrich. Ammonium hydroxide (50% v/v aqueous solution) and diiodomethane (99%) were supplied by Alfa Aesar. PEDOT:PSS (Clevios PVP AI4083) was provided by Heraeus. PTB7, PCDTBT, and $PC_{71}BM$ were bought from 1-Material Inc. PDPPTTT (M_w = 75000, PDI = 5.4) was synthesized under standard microwave Stille coupling conditions.[69] Evaporation materials (99.9% LiF, 99% Ca, 99.99% Al, 99.99% Au, 99.99% MgF_2, and 99.95% MoO_3) were obtained from Kurt J. Lesker. Prepatterned ITO substrates (10 Ω/square) were sourced from Thin Film Devices. All chemicals were used as received without further purification.

CuSCN Solutions and Thin Films: CuSCN was mixed with all solvents at a concentration of 10 mg mL^{-1}, and all solutions were filtered through 0.45 µm polytetrafluoroethylene (PTFE) filters before use. For DES, DPS, and NH_4OH, the solutions were stirred at room temperature for over 12 h, while for DMSO, DMF, and NMP, dissolution required heating at 120 °C for over 24 h with vigorous stirring. In the case of DMF and NMP the added CuSCN did not fully dissolve; the actual concentration was therefore determined by decanting a fixed portion of the solution, evaporating the solvent, and weighing the resulting precipitate.

CuSCN thin films were spin-coated on different substrates depending on the experiment being undertaken. All substrates were cleaned in ultrasonic baths first with acetone and then isopropanol for 10 min each, followed by UV–ozone treatment for 10 min. To achieve a comparable thickness for all samples, CuSCN-DES and CuSCN-DPS solutions were diluted to 3 and 4 mg mL^{-1}, respectively. Then all solutions were spin-coated at 1000 rpm. For high-boiling-point solvents, i.e., DMSO, DMF, and NMP, a long spinning time (3 min) was used to provide sufficient time for evaporation. Finally, the samples were annealed at 100 °C for 10 min in air, leading to ≈10 nm thickness films for all solvents except DMF and NMP where ≈6 nm thickness resulted. The spin-coating protocols were kept unchanged throughout this work unless otherwise stated.

Atomic Force Microscopy: CuSCN and PEDOT:PSS thin films were spin-coated on precleaned ITO substrates. For PEDOT:PSS, the spin speed was 2500 rpm, and the film was annealed at 150 °C for 15 min in air. (The same fabrication conditions were used for all PEDOT:PSS layers in this work.) The AFM topography and roughness were measured on an Asylum Research MFP-3D microscope with a Tap190Al-G cantilever (Budget Sensors). The measurement area was 2 × 2 $µm^2$. All data were processed using Gwyddion software.[71]

Raman Spectroscopy, Fourier-Transform Infrared Spectroscopy, and X-Ray Diffraction: Raman, FTIR and XRD measurements require relatively thick samples in order to acquire a sufficient signal-to-noise ratio. Therefore, CuSCN layers were deposited by drop-casting on different substrates (silicon for Raman and FTIR and glass for XRD). Raman spectroscopy was carried out with a Jobin Yvon T64000 triple spectrometer, calibrated by a silicon substrate before each measurement. Samples were excited by a Ventus solo Nd:YAG laser (λ = 532 nm). The triple spectrometer uses the first two gratings to reject the light at the excitation frequency, and the third to spatially disperse the Raman signal from the sample, which is collected by an Andor DU420A-OE charge-coupled device (CCD). The power output of the laser was controlled to achieve an incident radiation of <1 mW on the samples.

FTIR spectra were recorded with a Thermo Scientific Nicolet iS 5 spectrometer with iD5 accessory, and were measured in reflection mode. The contributions from air (primarily H_2O and CO_2) and the substrate were subtracted, and 32 scans were averaged for each sample.

Thin-film XRD were performed on a Rigaku SmartLab diffractometer with Cu Kα radiation (λ = 1.5406 Å) and a HyPix-3000 detector. The incident optics were in parallel-beam (PB) geometry with a 2.5° soller slit. The scans were carried out in the θ–θ configuration with a rotation rate of 1° min^{-1}. Background signals from the glass substrates were collected and subtracted.

X-Ray Photoelectron Spectroscopy: CuSCN thin films were spin-coated on precleaned fused silica substrates. Samples were analyzed using a Thermo Scientific K-Alpha XPS instrument equipped with a microfocused monochromated Al X-ray source ($h\nu$ = 1486.6 eV), and a 400 $µm^2$ spot size was used. The analyzer operated at a constant pass energy of 200 eV for survey scans and 50 eV for core level scans. Charge neutralization was applied using a dual-beam low-energy electron/ion flood source. The data acquisition was performed on Thermo Scientific Avantage software, and analysis was completed using CasaXPS software (Casa Software Ltd). All spectra were calibrated by the C 1s peak of adventitious carbon at a binding energy of 284.80 eV.

Surface Energy, Polymer Orientation, and Mobility Characterization: CuSCN thin films for surface energy measurements were spin-coated on precleaned ITO substrates. Droplets of the test liquids, deionized water and diiodomethane, were placed on the CuSCN surfaces, and images were recorded using an Ossila L2004A1 contact angle goniometer. Contact angle values were then extracted using Ossila Contact Angle software, and surface energies were calculated according to Fowkes theory.[53–54]

Grazing-incidence wide-angle X-ray scattering (GIWAXS) measurements were performed on ITO/CuSCN/PTB7 samples to assess the PTB7 crystallite orientation within the ≈100 nm thickness films spin-coated from 20 mg mL^{-1} chlorobenzene solution at 1000 rpm. Data were collected on a Rigaku SmartLab diffractometer using Cu Kα radiation

(λ = 1.5406 Å) and a HyPix-3000 2D detector. The incidence angle was 0.2°, and the exposure time was 30 min.

PTB7 hole mobility was measured using the MIS-CELIV method[58–59] on device structures comprising ITO/CuSCN/PTB7/MgF_2 (15 nm)/Al (100 nm). PTB7 layers were deposited using the same conditions as for GIWAXS samples, and MgF_2 and Al were thermally evaporated on top at 0.2 and 1 Å s^{-1}, respectively. MIS-CELIV experiments were performed using the Fluxim PAIOS measurement platform with Characterization Suite 4.2 software. The offset voltage was 5 V, and the voltage ramp rates were changed from 200 to 1000 V ms^{-1} with 200 V ms^{-1} steps.

Energy Level Measurements and Hole Injection Characteristics: Ionization potentials (IPs) of CuSCN thin films (spin-coated on precleaned ITO substrates) were measured by air photoemission spectroscopy (APS) using a KP Technology APS04 system. The tip potential was set to 10 V. The IP values were extracted from the intersection of the background and a linear fit to the cube root of the photoemission yield.[61–62] Absorbance spectra of CuSCN thin films (spin-coated on precleaned fused silica substrates) were used to derive optical gap energies using a PerkinElmer Lambda 1050 UV–vis–NIR spectrometer. The measured transmission (T) of all samples was converted to absorbance (A) by $A = -\log T$, from which the absorption coefficient α (in cm^{-1}) can be obtained given the known layer thickness. Tauc plots were used to study indirect $((\alpha h\nu)^{0.5}$ versus $h\nu$) and direct $((\alpha h\nu)^2$ versus $h\nu$) band gap energies.[63] Electron affinities (EAs) were estimated by subtracting the optical band gaps from the IP values, under the assumption that the band gap is direct and optical and electrical gaps are the same (small exciton binding energy). Work functions (WFs) of the CuSCN thin films (spin-coated on precleaned ITO substrates) were characterized using a KP Technology KP020 Kelvin probe with a gold disk tip (2 mm diameter). The measurements were performed in air, and the WF of the tip was calibrated using a highly oriented pyrolytic graphite (HOPG) reference whose WF is 4.650 eV. For each sample, more than 50 data points of contact potential difference between the tip and the sample were averaged.

PCDTBT-based hole-only diodes, with structure ITO/CuSCN/PCDTBT/MoO_3 (10 nm)/Al (100 nm), were fabricated to examine the difference in hole injection properties of the CuSCN interlayers. PCDTBT was dissolved in chlorobenzene at a concentration of 8 mg mL^{-1}, and was spin-coated on top of ITO/CuSCN in a N_2-filled glovebox at 1000 rpm, resulting in ≈85 nm thickness layers. Top electrodes were deposited by thermal evaporation at ≈10^{-6} Pa, with a rate of 0.2 Å s^{-1} for MoO_3 and 1 Å s^{-1} for Al. The *J–V* measurements were carried out in air using a Keithley 2400 sourcemeter. The MoO_3/Al electrode was defined as the cathode (held at negative bias relative to the ITO electrode) so that the hole injection properties of the different CuSCN interlayers could be compared from the observed current density under forward bias.

Polymer Light-Emitting Diode Fabrication and Characterization: The OLED structure used in this study was ITO/PEDOT:PSS or CuSCN/SY (≈90 nm)/LiF (1 nm)/Al (100 nm). The SY layers were spin-coated in a N_2-filled glovebox from 5 mg mL^{-1} toluene solution at 1500 rpm, followed by thermal annealing at 80 °C for 10 min. Then the SY-coated samples were transferred to a thermal evaporator to deposit a LiF (0.2 Å s^{-1})/Al (1 Å s^{-1}) bilayer cathode at ≈10^{-6} Pa. The device area was 15 mm^2, defined by the intersection of the ITO pattern and the shadow-mask-defined cathode. All OLED devices were encapsulated using UV-cured epoxy adhesive (Lumtec LT-U001) and glass coverslips before being brought out of the glovebox.

OLEDs were characterized using a custom-built setup, consisting of a Keithley 2636 sourcemeter, an Ocean Optics Maya2000 Pro spectrometer, and a Newport Oriel Instruments 70682NS integrating sphere. Bespoke software was used to choose the device under test, perform measurements, and collect data.

Organic Solar Cell Fabrication and Characterization: PTB7:$PC_{71}BM$ solar cells were fabricated using conventional device structures, namely ITO/PEDOT:PSS or CuSCN/PTB7:$PC_{71}BM$ (≈110 nm)/Ca (10 nm)/Al (100 nm). The active materials, PTB7 (donor, D) and $PC_{71}BM$ (acceptor, A), were dissolved in chlorobenzene (with 3 vol% 1,8-diiodooctane additive) at a total concentration of 25 mg mL^{-1} (D:A = 2:3), and spin-coated in a N_2-filled glovebox at 1000 rpm, followed by thermal annealing at 80 °C for 10 min. The samples were then transferred to a thermal evaporator where Ca (0.2 Å s^{-1}) and Al (1 Å s^{-1}) were deposited at ≈10^{-6} Pa. All devices were brought out of the glovebox for measurements without encapsulation.

The *J–V* characteristics were recorded by a Keithley 2401 sourcemeter, in the dark and under AM1.5 irradiation from a Wavelabs SINUS-220 solar simulator. The illuminated area of each device was 25 mm^2 defined by apertures on the metal mask covering the device during measurements. Bespoke software was used to choose the device under test, perform measurements, and collect data.

Organic Field-Effect Transistor Fabrication and Characterization: OFETs were studied in the top-gate bottom-contact configuration. The source and drain (50 nm thickness Au) contacts were thermally evaporated at ≈10^{-6} Pa with a rate of 0.2 Å s^{-1} onto precleaned glass substrates. A shadow mask was used to define the channel length (50 µm) and width (2 mm). After the deposition of CuSCN interlayers, ≈30 nm thickness PDPPTTT layers were spin-coated on top from 10 mg mL^{-1} 1,2-dichlorobenzene solution at 2000 rpm in a N_2-filled glovebox, followed by thermal annealing at 150 °C for 10 min. Next, PMMA dielectric layers (≈350 nm) were deposited by spin-coating 40 mg mL^{-1} *n*-butyl acetate solution at 1500 rpm and baked at 60 °C for 30 min. Finally, all samples were loaded into a thermal evaporator for 80 nm thickness Al gate electrodes (1 Å s^{-1}) to be deposited at ≈10^{-6} Pa. The devices were then brought out of the glovebox for measurements in air using a Keithley 4200-SCS semiconductor parameter analyzer connected to a Cascade Microtech probe station.

Supporting Information

Supporting Information is available from the Wiley Online Library or from the author.

Acknowledgements

B.W. and D.D.C.B. thank the China Scholarship Council (CSC, No. 201700260029), Pacific Alliance Group (PAG), China Oxford Scholarship Fund (COSF), and King Abdullah University of Science and Technology (KAUST, No. 121053645) for studentship support. D.D.C.B. thanks the Jiangsu Industrial Technology Research Institute (JITRI) and the JITRI-Oxford IMPACT Institute for project funding (R57149/CN001). The authors further thank Professors Henry Snaith, Robin Nicholas, Harish Bhaskaran, and SeungNam Cha for access to facilities, and Yu Shu and Oxford Materials Characterisation Service (OMCS) for experimental assistance. Professor Thomas Anthopoulos is acknowledged for fruitful discussions.

Conflict of Interest

The authors declare no conflict of interest.

Data Availability Statement

Research data are not shared.

Keywords

copper(I) thiocyanate, device performance, hole-transport interlayers, organic electronics, solvent effects on CuSCN properties

Received: November 19, 2021
Revised: February 13, 2022
Published online: March 18, 2022

[1] a) C. W. Tang, S. A. VanSlyke, *Appl. Phys. Lett.* **1987**, *51*, 913; b) J. H. Burroughes, D. D. C. Bradley, A. R. Brown, R. N. Marks, K. Mackay, R. H. Friend, P. L. Burns, A. B. Holmes, *Nature* **1990**, *347*, 539.
[2] a) M. Zhang, L. Zhu, G. Zhou, T. Hao, C. Qiu, Z. Zhao, Q. Hu, B. W. Larson, H. Zhu, Z. Ma, Z. Tang, W. Feng, Y. Zhang, T. P. Russell, F. Liu, *Nat. Commun.* **2021**, *12*, 309; b) M. A. Green, E. D. Dunlop, J. Hohl-Ebinger, M. Yoshita, N. Kopidakis, X. Hao, *Prog. Photovoltaics* **2021**, *29*, 657.
[3] A. F. Paterson, S. Singh, K. J. Fallon, T. Hodsden, Y. Han, B. C. Schroeder, H. Bronstein, M. Heeney, I. McCulloch, T. D. Anthopoulos, *Adv. Mater.* **2018**, *30*, 1801079.
[4] a) H. Ma, H.-L. Yip, F. Huang, A. K. Y. Jen, *Adv. Funct. Mater.* **2010**, *20*, 1371; b) R. Sorrentino, E. Kozma, S. Luzzati, R. Po, *Energy Environ. Sci.* **2021**, *14*, 180.
[5] M. Fahlman, S. Fabiano, V. Gueskine, D. Simon, M. Berggren, X. Crispin, *Nat. Rev. Mater.* **2019**, *4*, 627.
[6] a) L. Chen, P. Degenaar, D. D. C. Bradley, *Adv. Mater.* **2008**, *20*, 1679; b) R. Jin, P. A. Levermore, J. Huang, X. Wang, D. D. C. Bradley, J. C. deMello, *Phys. Chem. Chem. Phys.* **2009**, *11*, 3455.
[7] a) S. Khodabakhsh, D. Poplavskyy, S. Heutz, J. Nelson, D. D. C. Bradley, H. Murata, T. S. Jones, *Adv. Funct. Mater.* **2004**, *14*, 1205; b) S. Nam, V. R. de la Rosa, Y. Cho, R. Hamilton, S. Cha, R. Hoogenboom, D. D. C. Bradley, *Appl. Phys. Lett.* **2019**, *115*, 143302; c) C.-m. Kang, J. Wade, S. Yun, J. Lim, H. Cho, J. Roh, H. Lee, S. Nam, D. D. C. Bradley, J.-S. Kim, C. Lee, *Adv. Electron. Mater.* **2016**, *2*, 1500282.
[8] a) Y. Zhou, C. Fuentes-Hernandez, J. Shim, J. Meyer, A. J. Giordano, H. Li, P. Winget, T. Papadopoulos, H. Cheun, J. Kim, M. Fenoll, A. Dindar, W. Haske, E. Najafabadi, T. M. Khan, H. Sojoudi, S. Barlow, S. Graham, J. L. Bredas, S. R. Marder, A. Kahn, B. Kippelen, *Science* **2012**, *336*, 327; b) C. Duan, K. Zhang, C. Zhong, F. Huang, Y. Cao, *Chem. Soc. Rev.* **2013**, *42*, 9071; c) Z. Liang, Q. Zhang, L. Jiang, G. Cao, *Energy Environ. Sci.* **2015**, *8*, 3442; d) S. Nam, J. Seo, S. Woo, W. H. Kim, H. Kim, D. D. C. Bradley, Y. Kim, *Nat. Commun.* **2015**, *6*, 8929; e) S. A. Haque, S. Koops, N. Tokmoldin, J. R. Durrant, J. Huang, D. D. C. Bradley, E. Palomares, *Adv. Mater.* **2007**, *19*, 683.
[9] a) P. A. Levermore, L. Chen, X. Wang, R. Das, D. D. C. Bradley, *Adv. Mater.* **2007**, *19*, 2379; b) X. Wang, T. Ishwara, W. Gong, M. Campoy-Quiles, J. Nelson, D. D. C. Bradley, *Adv. Funct. Mater.* **2012**, *22*, 1454.
[10] J. Meyer, S. Hamwi, M. Kroger, W. Kowalsky, T. Riedl, A. Kahn, *Adv. Mater.* **2012**, *24*, 5408.
[11] Y. Jiang, T. Liu, Y. Zhou, *Adv. Funct. Mater.* **2020**, *30*, 2006213.
[12] H. Shi, C. Liu, Q. Jiang, J. Xu, *Adv. Electron. Mater.* **2015**, *1*, 1500017.
[13] N. Koch, A. Vollmer, A. Elschner, *Appl. Phys. Lett.* **2007**, *90*, 043512.
[14] a) M. P. de Jong, L. J. van Ijzendoorn, M. J. A. de Voigt, *Appl. Phys. Lett.* **2000**, *77*, 2255; b) A. Garcia, G. C. Welch, E. L. Ratcliff, D. S. Ginley, G. C. Bazan, D. C. Olson, *Adv. Mater.* **2012**, *24*, 5368.
[15] a) A. Perumal, H. Faber, N. Yaacobi-Gross, P. Pattanasattayavong, C. Burgess, S. Jha, M. A. McLachlan, P. N. Stavrinou, T. D. Anthopoulos, D. D. C. Bradley, *Adv. Mater.* **2015**, *27*, 93; b) N. Yaacobi-Gross, N. D. Treat, P. Pattanasattayavong, H. Faber, A. K. Perumal, N. Stingelin, D. D. C. Bradley, P. N. Stavrinou, M. Heeney, T. D. Anthopoulos, *Adv. Energy Mater.* **2015**, *5*, 1401529.
[16] E. L. Ratcliff, B. Zacher, N. R. Armstrong, *J. Phys. Chem. Lett.* **2011**, *2*, 1337.
[17] D. Poplavskyy, J. Nelson, D. D. C. Bradley, *Appl. Phys. Lett.* **2003**, *83*, 707.
[18] N. B. Kotadiya, H. Lu, A. Mondal, Y. Ie, D. Andrienko, P. W. M. Blom, G. A. H. Wetzelaer, *Nat. Mater.* **2018**, *17*, 329.
[19] P. A. Lane, P. J. Brewer, J. Huang, D. D. C. Bradley, J. C. deMello, *Phys. Rev. B: Condens. Matter Mater. Phys.* **2006**, *74*, 125320.
[20] J. Huang, P. F. Miller, J. S. Wilson, A. J. de Mello, J. C. de Mello, D. D. C. Bradley, *Adv. Funct. Mater.* **2005**, *15*, 290.
[21] M. T. Greiner, L. Chai, M. G. Helander, W.-M. Tang, Z.-H. Lu, *Adv. Funct. Mater.* **2012**, *22*, 4557.
[22] F. Wang, Z. a. Tan, Y. Li, *Energy Environ. Sci.* **2015**, *8*, 1059.
[23] R. M. Pasquarelli, D. S. Ginley, R. O'Hayre, *Chem. Soc. Rev.* **2011**, *40*, 5406.
[24] a) E. L. Ratcliff, J. Meyer, K. X. Steirer, A. Garcia, J. J. Berry, D. S. Ginley, D. C. Olson, A. Kahn, N. R. Armstrong, *Chem. Mater.* **2011**, *23*, 4988; b) S. Ohisa, S. Kagami, Y. J. Pu, T. Chiba, J. Kido, *ACS Appl. Mater. Interfaces* **2016**, *8*, 20946.
[25] G. R. R. A. Kumara, A. Konno, G. K. R. Senadeera, P. V. V. Jayaweera, D. B. R. A. De Silva, K. Tennakone, *Sol. Energy Mater. Sol. Cells* **2001**, *69*, 195.
[26] a) J. E. Jaffe, T. C. Kaspar, T. C. Droubay, T. Varga, M. E. Bowden, G. J. Exarhos, *J. Phys. Chem. C* **2010**, *114*, 9111; b) P. Pattanasattayavong, V. Promarak, T. D. Anthopoulos, *Adv. Electron. Mater.* **2017**, *3*, 1600378.
[27] a) N. D. Treat, N. Yaacobi-Gross, H. Faber, A. K. Perumal, D. D. C. Bradley, N. Stingelin, T. D. Anthopoulos, *Appl. Phys. Lett.* **2015**, *107*, 013301; b) N. Chaudhary, R. Chaudhary, J. P. Kesari, A. Patra, S. Chand, *J. Mater. Chem. C* **2015**, *3*, 11886; c) N. Wijeyasinghe, T. D. Anthopoulos, *Semicond. Sci. Technol.* **2015**, *30*, 104002; d) N. Wijeyasinghe, A. Regoutz, F. Eisner, T. Du, L. Tsetseris, Y.-H. Lin, H. Faber, P. Pattanasattayavong, J. Li, F. Yan, M. A. McLachlan, D. J. Payne, M. Heeney, T. D. Anthopoulos, *Adv. Funct. Mater.* **2017**, *27*, 1701818; e) N. Chaudhary, R. Chaudhary, J. P. Kesari, A. Patra, *Opt. Mater.* **2017**, *69*, 367.
[28] R. G. Pearson, *J. Am. Chem. Soc.* **1963**, *85*, 3533.
[29] R. G. Parr, R. G. Pearson, *J. Am. Chem. Soc.* **1983**, *105*, 7512.
[30] T. V. Popova, N. V. Aksenova, *Russ. J. Coord. Chem.* **2003**, *29*, 743.
[31] M. Kabešová, M. Dunaj-jurčo, M. Serator, J. Gažo, J. Garaj, *Inorg. Chim. Acta* **1976**, *17*, 161.
[32] D. L. Smith, V. I. Saunders, *Acta Crystallogr., Sect. B: Struct. Sci., Cryst. Eng. Mater.* **1981**, *37*, 1807.
[33] L. Tsetseris, *J. Phys.: Condens. Matter* **2016**, *28*, 295801.
[34] L. Sun, Y. Huang, M. Anower Hossain, K. Li, S. Adams, Q. Wang, *J. Electrochem. Soc.* **2012**, *159*, D323.
[35] B. N. Ezealigo, A. C. Nwanya, A. Simo, R. Bucher, R. U. Osuji, M. Maaza, M. V. Reddy, F. I. Ezema, *Arabian J. Chem.* **2020**, *13*, 346.
[36] Y. Tsuda, H. Sun, L. Sun, S. Okada, A. Masuhara, P. Stadler, N. S. Sariciftci, M. S. White, T. Yoshida, *Monatsh. Chem.* **2017**, *148*, 845.
[37] L. Tsetseris, *Phys. Chem. Chem. Phys.* **2016**, *18*, 7837.
[38] a) D. Aldakov, C. Chappaz-Gillot, R. Salazar, V. Delaye, K. A. Welsby, V. Ivanova, P. R. Dunstan, *J. Phys. Chem. C* **2014**, *118*, 16095; b) G. A. Bowmaker, J. V. Hanna, *Z. Naturforsch., B: J. Chem. Sci.* **2009**, *64*, 1478.
[39] S. Gates-Rector, T. Blanton, *Powder Diffr.* **2019**, *34*, 352.
[40] P. Pattanasattayavong, G. O. Ndjawa, K. Zhao, K. W. Chou, N. Yaacobi-Gross, B. C. O'Regan, A. Amassian, T. D. Anthopoulos, *Chem. Commun.* **2013**, *49*, 4154.
[41] a) G. Ayala, R. D. Pike, *Polyhedron* **2016**, *115*, 242; b) P. Worakajit, F. Hamada, D. Sahu, P. Kidkhunthod, T. Sudyoadsuk, V. Promarak, D. J. Harding, D. M. Packwood, A. Saeki, P. Pattanasattayavong, *Adv. Funct. Mater.* **2020**, *30*, 2002355.
[42] K. H. Schulz, D. F. Cox, *J. Phys. Chem.* **1993**, *97*, 3555.
[43] N. Wijeyasinghe, F. Eisner, L. Tsetseris, Y.-H. Lin, A. Seitkhan, J. Li, F. Yan, O. Solomeshch, N. Tessler, P. Patsalas, T. D. Anthopoulos, *Adv. Funct. Mater.* **2018**, *28*, 1802055.
[44] J. Wei, Q. Xue, *Wear* **1994**, *176*, 213.
[45] J. C. Klein, C. P. Li, D. M. Hercules, J. F. Black, *Appl. Spectrosc.* **1984**, *38*, 729.
[46] M. C. Biesinger, *Surf. Interface Anal.* **2017**, *49*, 1325.
[47] C. E. Dubé, B. Workie, S. P. Kounaves, A. Robbat, M. L. Aksub, G. Davies, *J. Electrochem. Soc.* **1995**, *142*, 3357.

[48] D. K. Zhang, Y. C. Liu, Y. L. Liu, H. Yang, *Phys. B(Amsterdam, Neth.)* **2004**, *351*, 178.
[49] J. Kim, Y. Lee, B. Gil, A. J. Yun, J. Kim, H. Woo, K. Park, B. Park, *ACS Appl. Energy Mater.* **2020**, *3*, 7572.
[50] I. Osaka, K. Takimiya, *Polymer* **2015**, *59*, A1.
[51] a) T. Umeda, D. Kumaki, S. Tokito, *J. Appl. Phys.* **2009**, *105*, 024516; b) X. Zhang, L. J. Richter, D. M. DeLongchamp, R. J. Kline, M. R. Hammond, I. McCulloch, M. Heeney, R. S. Ashraf, J. N. Smith, T. D. Anthopoulos, B. Schroeder, Y. H. Geerts, D. A. Fischer, M. F. Toney, *J. Am. Chem. Soc.* **2011**, *133*, 15073.
[52] Y. Liang, Z. Xu, J. Xia, S. T. Tsai, Y. Wu, G. Li, C. Ray, L. Yu, *Adv. Mater.* **2010**, *22*, E135.
[53] F. M. Fowkes, *Ind. Eng. Chem.* **1964**, *56*, 40.
[54] A. Kozbial, Z. Li, C. Conaway, R. McGinley, S. Dhingra, V. Vahdat, F. Zhou, B. D'Urso, H. Liu, L. Li, *Langmuir* **2014**, *30*, 8598.
[55] C. J. van Oss, *Interfacial Forces in Aqueous Media*, CRC Press, Boca Raton, FL **2006**.
[56] K. J. Chen, A. D. Laurent, F. Boucher, F. Odobel, D. Jacquemin, *J. Mater. Chem. A* **2016**, *4*, 2217.
[57] V. Savikhin, L. K. Jagadamma, L. J. Purvis, I. Robertson, S. D. Oosterhout, C. J. Douglas, I. D. W. Samuel, M. F. Toney, *iScience* **2018**, *2*, 182.
[58] G. Juška, N. Nekrašas, K. Genevičius, *J. Non-Cryst. Solids* **2012**, *358*, 748.
[59] a) A. Armin, G. Juska, M. Ullah, M. Velusamy, P. L. Burn, P. Meredith, A. Pivrikas, *Adv. Energy Mater.* **2014**, *4*, 1300954; b) B. Wang, H. Ye, M. Riede, D. D. C. Bradley, *ACS Appl. Mater. Interfaces* **2021**, *13*, 2919.
[60] S. Foster, F. Deledalle, A. Mitani, T. Kimura, K.-B. Kim, T. Okachi, T. Kirchartz, J. Oguma, K. Miyake, J. R. Durrant, S. Doi, J. Nelson, *Adv. Energy Mater.* **2014**, *4*, 1400311.
[61] Y. Peng, N. Yaacobi-Gross, A. K. Perumal, H. A. Faber, G. Vourlias, P. A. Patsalas, D. D. C. Bradley, Z. He, T. D. Anthopoulos, *Appl. Phys. Lett.* **2015**, *106*, 243302.
[62] R. H. Fowler, *Phys. Rev.* **1931**, *38*, 45.
[63] J. Tauc, R. Grigorovici, A. Vancu, *Phys. Status Solidi B* **1966**, *15*, 627.
[64] J.-L. Brédas, *Mater. Horiz.* **2014**, *1*, 17.
[65] W. Melitz, J. Shen, A. C. Kummel, S. Lee, *Surf. Sci. Rep.* **2011**, *66*, 1.
[66] S. Braun, W. R. Salaneck, M. Fahlman, *Adv. Mater.* **2009**, *21*, 1450.
[67] F. Lombeck, D. Di, L. Yang, L. Meraldi, S. Athanasopoulos, D. Credgington, M. Sommer, R. H. Friend, *Macromolecules* **2016**, *49*, 9382.
[68] S. R. Forrest, D. D. C. Bradley, M. E. Thompson, *Adv. Mater.* **2003**, *15*, 1043.
[69] S. Nam, H. Han, J. Seo, M. Song, H. Kim, T. D. Anthopoulos, I. McCulloch, D. D. C. Bradley, Y. Kim, *Adv. Electron. Mater.* **2016**, *2*, 1600264.
[70] B. de Boer, A. Hadipour, M. M. Mandoc, T. van Woudenbergh, P. W. M. Blom, *Adv. Mater.* **2005**, *17*, 621.
[71] D. Nečas, P. Klapetek, *Cent. Eur. J. Phys.* **2012**, *10*, 181.